Small-scale behavior in distorted turbulent boundary layers at low Reynolds number

By Seyed G. Saddoughi

1. Motivation and background

During the last three years (Saddoughi 1993a; Saddoughi 1993b; Saddoughi & Veeravalli 1994), we have conducted high- and low-Reynolds-number experiments, including hot-wire measurements of the velocity fluctuations, in the test-section-ceiling boundary layer of the 80- by 120-foot Full-Scale Aerodynamics Facility at NASA Ames Research Center, to test the local-isotropy predictions of Kolmogorov's (1941) universal equilibrium theory. This hypothesis, which states that at sufficiently high Reynolds numbers the small-scale structures of turbulent motions are independent of large-scale structures and mean deformations, has been used in theoretical studies of turbulence and computational methods such as large-eddy simulation: however, its range of validity in shear flows has been a subject of controversy. The present experiments were planned to enhance our understanding of the local-isotropy hypothesis.

Our experiments were divided into two sets. First, (Saddoughi & Veeravalli 1994) measurements were taken at different Reynolds numbers in a plane boundary layer, which is a "simple" shear flow with the basic mean strain rate $S \equiv \partial U/\partial y$. Here our results established the conditions under which local isotropy can be expected in simple shear flows. Detailed analyses of these data have been already presented in our previous reports. The main conclusions were that the lower-wavenumber limit of locally-isotropic behavior (negligible shear-stress cospectra) is given by $k_1\sqrt{\varepsilon/S^3} \approx 10$. Our investigation also indicated that for energy spectra this limit could be relaxed to $k_1\sqrt{\varepsilon/S^3} \approx 3$; this is Corrsin's (1958) criterion, with the numerical value obtained from our data. The existence of an isotropic inertial range requires that this wavenumber be much less than the wavenumber at the onset of viscous effects so that the combined condition (Corrsin 1958 and Uberoi 1957) is $S\sqrt{\nu/\varepsilon} \ll 1$. Spectral "bumps" between the $-5/3$ inertial range and the dissipative range were observed on all the compensated energy spectra. The shear-stress cospectra rolled off with a $-7/3$ power law and scaled linearly with S (Lumley 1967). In summary, it was shown that one decade of inertial subrange with truly negligible shear-stress co-spectral density requires $S\sqrt{\nu/\varepsilon}$ not more than about 0.01 (for a shear layer with turbulent kinetic energy production approximately equal to dissipation, this implies a microscale Reynolds number of about 1500).

Second, experiments were designed to address this question: will our criteria for the existence of local isotropy hold for "complex" non-equilibrium flows in which extra rates of mean strain are added to the basic mean shear. In our last report (Saddoughi 1993b) we showed that the small-scale data taken at different locations in a highly-distorted boundary layer at high microscale Reynolds numbers (1750

to 2000) behaved similarly to the simple shear flow case, and that they satisfied the local-isotropy predictions. In the current report the results of our experiments conducted in complex flows at low Reynolds numbers at a variety of extra mean strain rates are presented.

2. Accomplishments

2.1 Apparatus and measurement techniques

We have studied the plane-of-symmetry flow in front of a circular cylinder placed vertically in a fully developed two-dimensional turbulent boundary layer. In this type of flow, the pressure rises strongly as the obstacle is approached, and the boundary layer is also influenced by the effects of lateral divergence. Hence, in addition to the basic mean shear, $\partial U/\partial y$, the extra mean strain rates involved in the flow are $\partial U/\partial x$, $\partial V/\partial y$, and $\partial W/\partial z$. To obtain the desired effects, the size of the cylinder should be at least of the order of the thickness of the boundary layer. Since in our study the approaching boundary-layer thickness was approximately 1.1 m, the following dimensions were chosen for our test cylinder: D = 1.22 m and height L = 1.83 m. Our measurement location was fixed at $x/D \approx 0.85$ with respect to the front of the cylinder.

We presented (Saddoughi 1993b) a very brief review of the experimental investigations dealing with the large-scale structural changes that occur in this kind of flow, and also gave a detailed description of the test cylinder and other apparatus used in our experiments. The measurement strategy, instrumentation, and procedure were all similar to those explained by Saddoughi & Veeravalli (1994), and details will not be repeated here.

Our low-Reynolds-number complex-flow experiments are divided into two cases: boundary layers under the influence of (i) large and (ii) small, extra mean strain rates. These two flow cases are described below.

2.2 Distorted boundary layers: Large extra-strain-rate experiments

Fig. 1. shows a schematic diagram of the test cylinder attached to the ceiling of the $80' \times 120'$ wind tunnel. During our complex-flow measurements the tunnel runs were dedicated to our experiments; however, as shown in Fig. 1, a full-scale F-18 fighter aircraft set at an angle of attack of 50° was present in the central region of the working section for both the high- and low-Reynolds-number measurements. It will be shown later that the presence of the aircraft in the tunnel usefully increased the mean strain rate in front of the cylinder.

Our low-Reynolds-number measurements have been taken at a reference velocity, $U_{ref} = 10.75$ m/s. The mean-flow data for this case are compared with the data for the high-Reynolds-number large-extra-strain-rate case in Fig. 2.

The normalized profiles of the longitudinal mean velocity, U/U_{ref}, for the distorted boundary layers are compared with the profiles obtained for the plane boundary layer in Fig. 2(a), where y is the distance from the wall. The shapes of the velocity profiles for the distorted boundary layers are typical of the large adverse-pressure-gradient flows: note the flattening of the profiles in the middle of the layer.

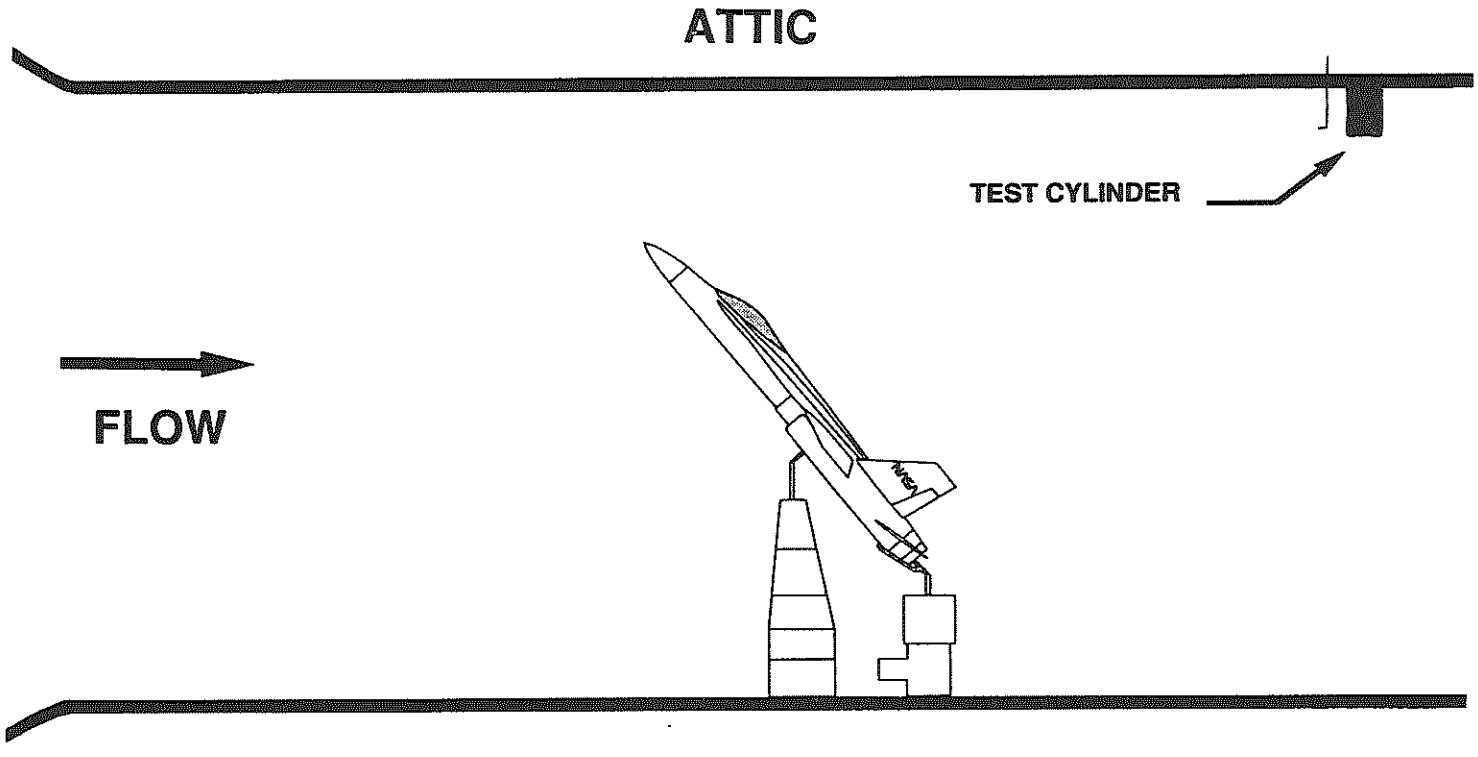

FIGURE 1. A schematic diagram for the large extra-strain-rate experiments, showing the relative position of the test cylinder with respect to the F-18 aircraft, which is set at an angle of attack $\alpha \approx 50°$. The drawing is to scale.

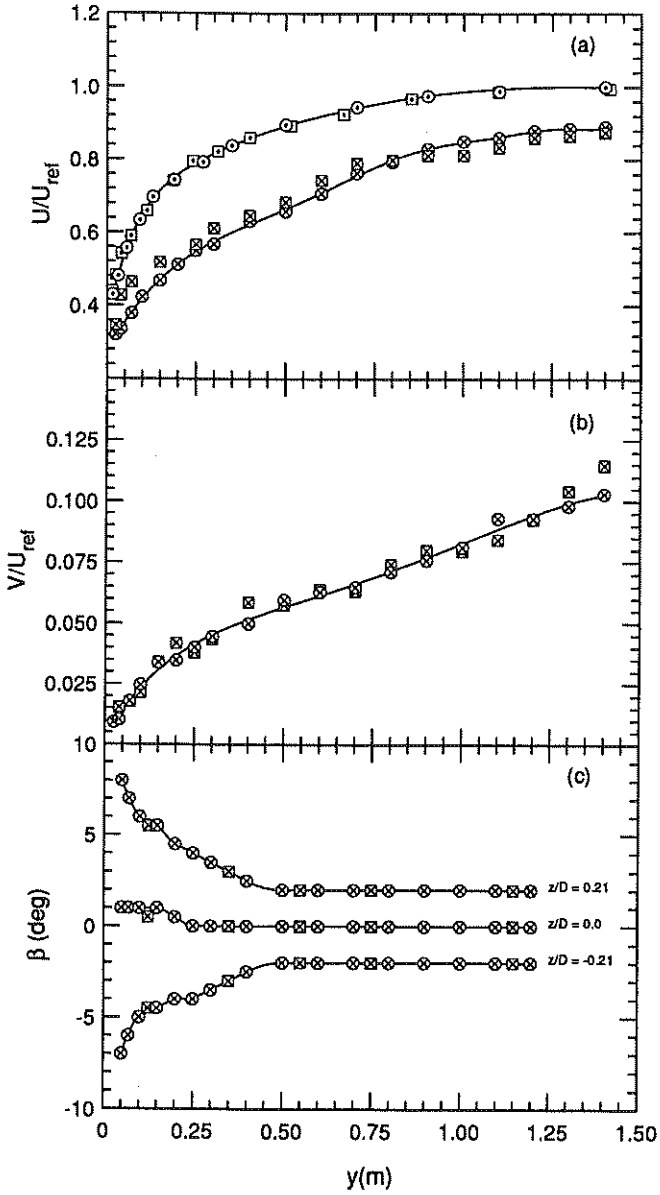

FIGURE 2. Mean-flow data at high and low Reynolds numbers. (a) Normalized longitudinal mean-velocity profiles, U/U_{ref}, measured in large extra-strain-rate and plane boundary layers. (b) Normalized vertical mean-velocity profiles, V/U_{ref}, measured in large extra-strain-rate boundary layers. (c) Flow yaw-angle profiles, β, measured in large extra-strain-rate boundary layers at different spanwise locations. ⊙ , $U_{ref} \approx 50$ m/s and ⊡ , $U_{ref} \approx 10$ m/s plane boundary layer; ⊗ , $U_{ref} \approx 51.25$ m/s and ⊠ , $U_{ref} \approx 10.75$ m/s large extra-strain-rate boundary layer.

The boundary-layer thickness, δ (the point where $U/U_e = 0.995$), has increased to approximately 1250 mm in the distorted boundary layer. Here the shape factor $H \approx 1.85$, and at the edge of the boundary layer the pressure coefficient $C_p \approx 0.23$.

Fig. 2(b) shows the normalized profiles of the vertical velocity component, V/U_{ref}. A least-squares polynomial fit to the V profile was used to obtain the values of $\partial V/\partial y$.

The magnitudes of the extra strain rate due to the streamline divergence, $\partial W/\partial z$, influencing the plane of symmetry of the flow can be obtained from $(\partial W/\partial z) \equiv U(\partial\beta/\partial z)$ (see e.g. Saddoughi & Joubert 1991), where β is the flow yaw angle measured at different spanwise locations z. The profiles of β measured by a yaw-meter probe for three spanwise locations ($z/D = -0.21$, 0, and 0.21) through the boundary layers are shown in Fig. 2(c). It can be seen that, as expected, in the plane of symmetry of the flow the crossflow, W, is approximately equal to zero. The profiles are typical of three-dimensional boundary layers: larger flow yaw angles near the wall than the freestream.

Finally, the continuity equation was used to obtain the $\partial U/\partial x$ values. For both our high and low Reynolds number distorted boundary layers, typical values of $(\partial U/\partial x)/(\partial U/\partial y)$, $(\partial V/\partial y)/(\partial U/\partial y)$, and $(\partial W/\partial z)/(\partial U/\partial y)$ were larger than 0.1, 0.2, and 0.3 respectively. These large extra-mean-strain rates produce large non-linear effects on the large-scale structures of the boundary layers (Bradshaw 1973).

The profiles of the Reynolds normal stresses $(\overline{u_1^2}/U_{ref}^2, \overline{u_2^2}/U_{ref}^2, \overline{u_3^2}/U_{ref}^2)$, and the shear stress, $-\overline{u_1u_2}/U_{ref}^2$, for the distorted boundary layers at high and low Reynolds numbers are compared with the profiles for the plane boundary layers in Fig. 3. The profiles for the distorted boundary layers appear to be quite different from the plane flow case. The peaks of $\overline{u_2^2}$ and the shear stress, $-\overline{u_1u_2}$, profiles have moved away from the wall to $y \approx 300$ mm, and in the outer part of the layer the values of all the Reynolds stresses have increased.

From Fig. 3(d) it can be deduced that at the wall $\tau/\rho U_{ref}^2 \approx 0.0003$. Also from Fig. 2(a) note that at the edge of the boundary layer $U/U_{ref} \approx 0.88$. Based on the above values, a $C_f \approx 0.00078$ can be obtained, which corresponds to shear velocities $U_\tau \approx 0.89$ m/s and 0.186 m/s for the high-Reynolds-number and low-Reynolds-number cases respectively. Using U_τ as the scaling velocity, the Reynolds shear-stress profiles are replotted in Fig. 4. These large changes in the large-scale structure of turbulence are due to the effects of large adverse pressure gradients (see Bradshaw 1967).

2.2.1 Analysis of small-scale data: low-Reynolds-number case

As mentioned earlier, the spectral measurements taken in this highly-distorted boundary layer at high Reynolds number were presented in our last report where it was shown that these data satisfied local-isotropy predictions. Hence, in the following we will concentrate only on the low-Reynolds-number experiments.

The spectral measurements of the three components of the velocity taken at $y = 100$ mm (inner-layer), 300 mm (maximum shear stress), 500 mm (around mid-layer), and 700 mm (outer-layer) for the low-speed case are analyzed here. In this case, the microscale Reynolds number range was about 850 to 650.

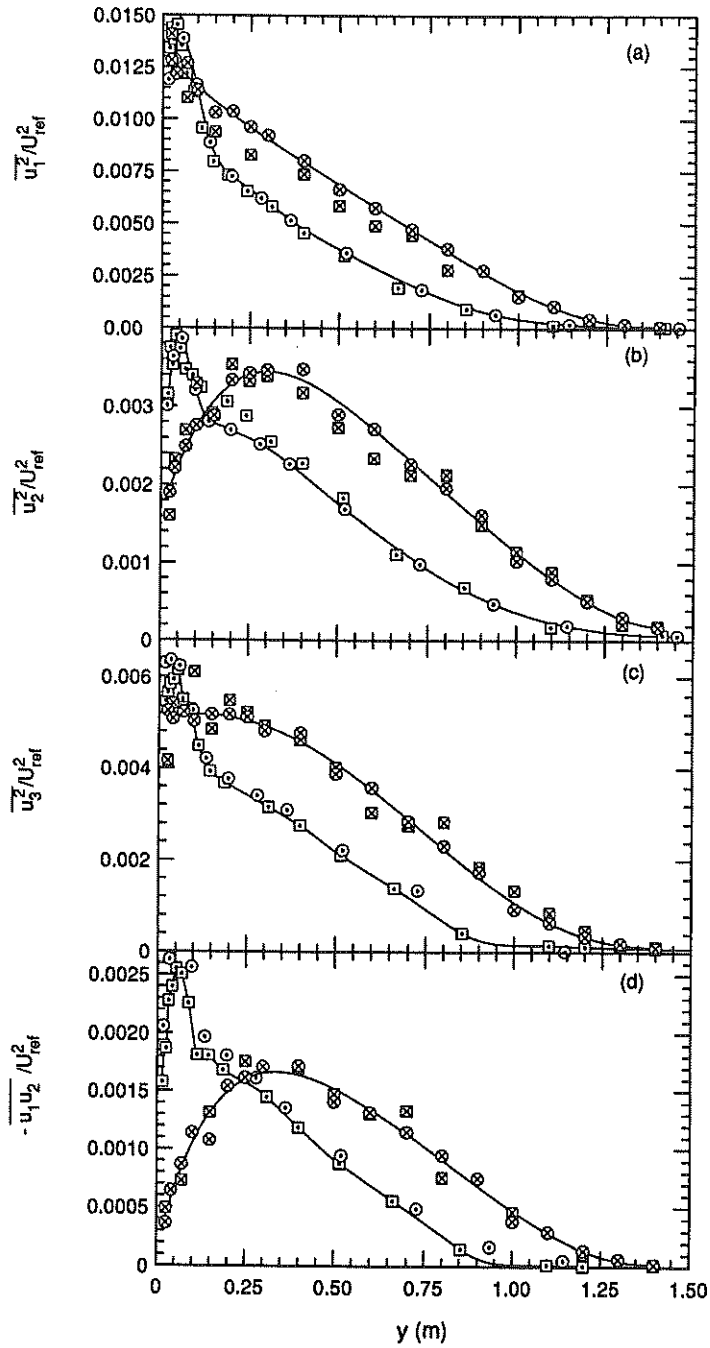

FIGURE 3. Profiles of Reynolds stresses measured in plane and large extra-strain-rate boundary layers at high and low Reynolds numbers: (a) $\overline{u_1^2}/U_{ref}^2$, (b) $\overline{u_2^2}/U_{ref}^2$, (c) $\overline{u_3^2}/U_{ref}^2$, (d) $-\overline{u_1u_2}/U_{ref}^2$. For key to symbols see Fig. 2.

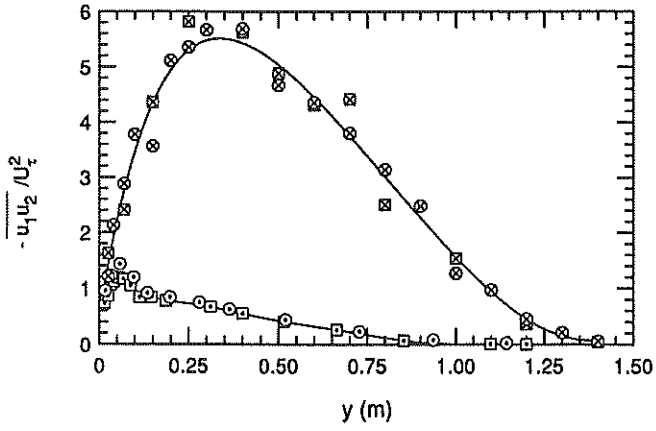

FIGURE 4. Scaling of the Reynolds shear-stress profiles (Fig. 3d) using U_τ as velocity scale. For key to symbols see Fig. 2.

Compensated spectra can be defined as $\varepsilon^{-2/3}k_1^{5/3}E_{\alpha\alpha}(k_1)$, where $\alpha = 1$, 2 or 3 (no summation over α). In the inertial subrange, these should be independent of wavenumber and equal to the Kolmogorov's constants for one-dimensional spectra.

In Fig. 5 the compensated longitudinal spectra at the four y-positions are plotted against $k_1\eta$. The compensated ninth-order, least-square log-log polynomial fits of $E_{11}(k_1)$ are also presented in this figure. Here the dissipation value at each measurement location was obtained from the isotropic relation $\varepsilon = 15\nu \int_0^\infty k_1^2 E_{11}(k_1)dk_1$ (e.g. Batchelor 1953). (For details see our previous reports.) As can be seen in this figure, the u_1-spectra (single wire) at all the measurement locations have -5/3 ranges and the Kolmogorov constant $C = 1.5$ (*i.e.* $C_1 = 18C/55 = 0.491$) (Monin & Yaglom 1975; Saddoughi & Veeravalli 1994) agrees reasonably well with the present data.

The compensated u_2- and u_3-spectra are presented in Figs. 6 and 7 respectively. These two figures illustrate several points. (i) They show that the extent of $-5/3$ range of the transverse spectra reduces when the wall is approached. This is similar to the behavior of the spectra for the zero-pressure-gradient boundary layer. (ii) At the inner-layer position, isotropy is satisfied and the densities of the transverse spectra in the inertial subrange are equal to 4/3 times that of the u_1-spectrum. However, when the outer part of the boundary layer is approached, there is an increased deviation from isotropic behavior. (iii) All the compensated spectra at the outer-layer position (y = 700 mm) have a new "bump" between the large-scale range and the inertial subrange. (iv) At all the measurement positions, to within the accuracy of measurement, the u_3- and u_2-spectra are equal to each other in the inertial subrange and dissipation range. This is further illustrated in Fig. 8, where the ratio of the measured u_3-spectrum to u_2-spectrum, $E_{33}^{meas}(k_1)/E_{22}^{meas}(k_1)$, at each y location is plotted against $k_1\eta$.

All of the above measurements were repeated by taking data on different days with different hot-wire elements having different calibrations and using different anemometers. Also, the u_1-spectra obtained by X-wires in x-y and x-z planes

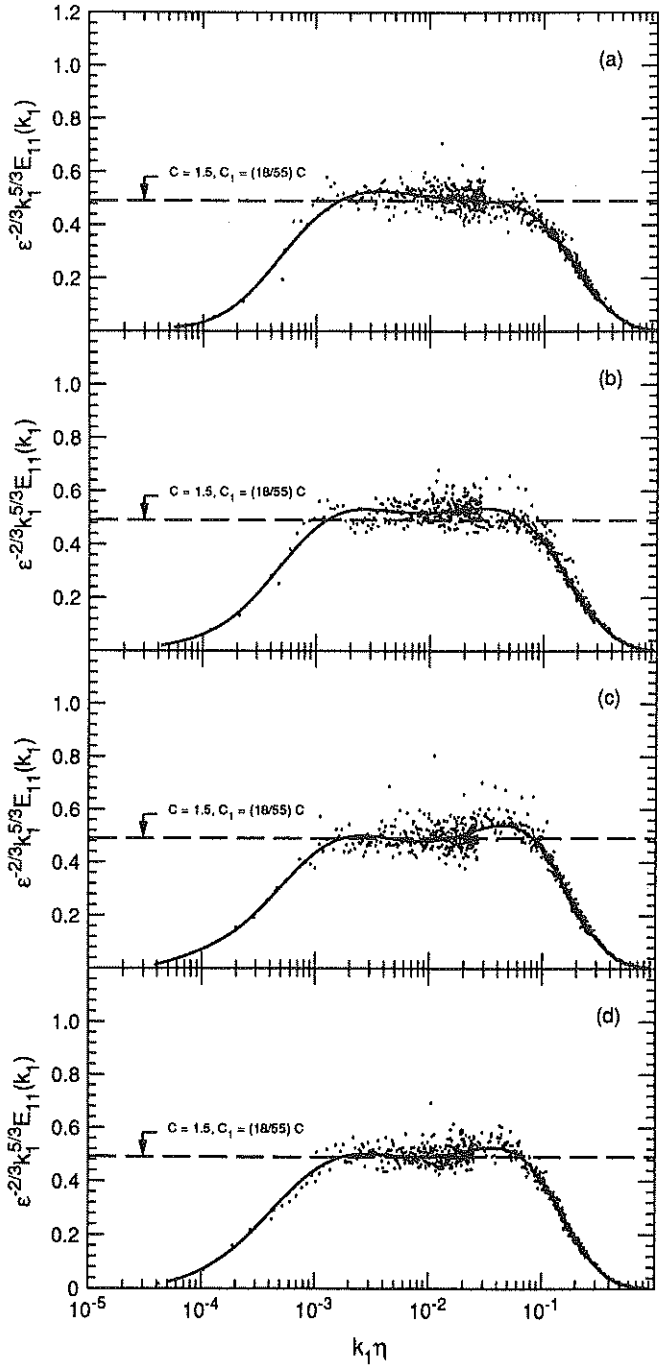

FIGURE 5. Compensated u_1-spectra measured at different locations in the large extra-strain-rate boundary layer at low Reynolds number. Solid lines are the ninth-order, least-square, log-log polynomial fits to the spectral data. (a) $y = 700$ mm (outer-layer), $R_\lambda \approx 650$; (b) $y = 500$ mm (around mid-layer), $R_\lambda \approx 820$; (c) $y = 300$ mm (maximum shear stress), $R_\lambda \approx 800$; (d) $y = 100$ mm (inner-layer), $R_\lambda \approx 830$.

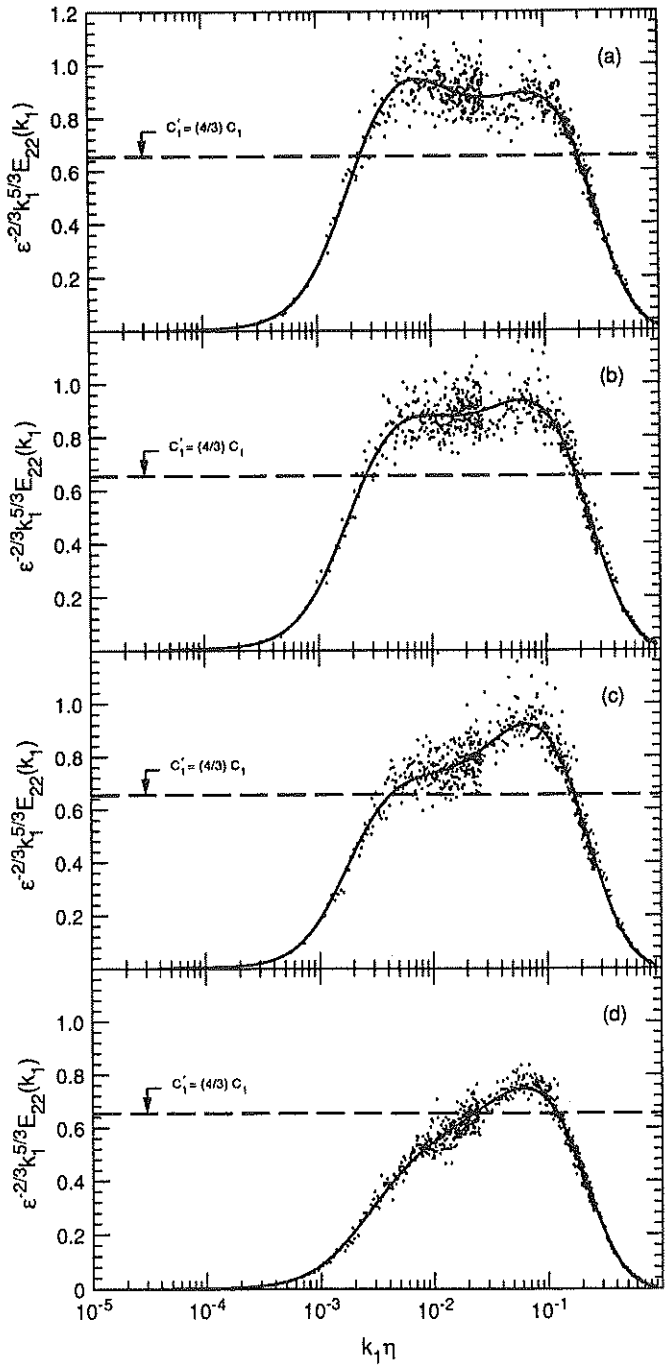

FIGURE 6. Compensated u_2-spectra measured at different locations in the large extra-strain-rate boundary layer at low Reynolds number. Solid lines are the ninth-order, least-square, log-log polynomial fits to the spectral data. For key to captions for (a)-(d) see Fig. 5.

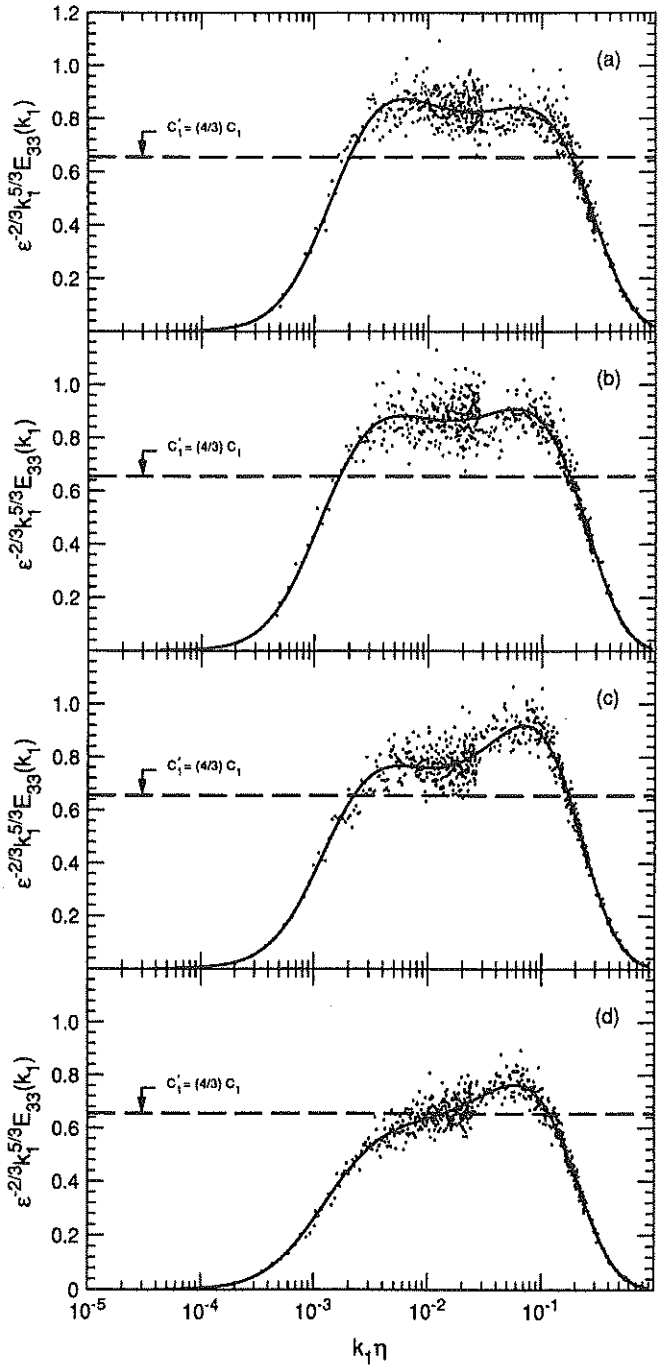

FIGURE 7. Compensated u_3-spectra measured at different locations in the large extra-strain-rate boundary layer at low Reynolds number. Solid lines are the ninth-order, least-square, log-log polynomial fits to the spectral data. For key to captions for (a)-(d) see Fig. 5.

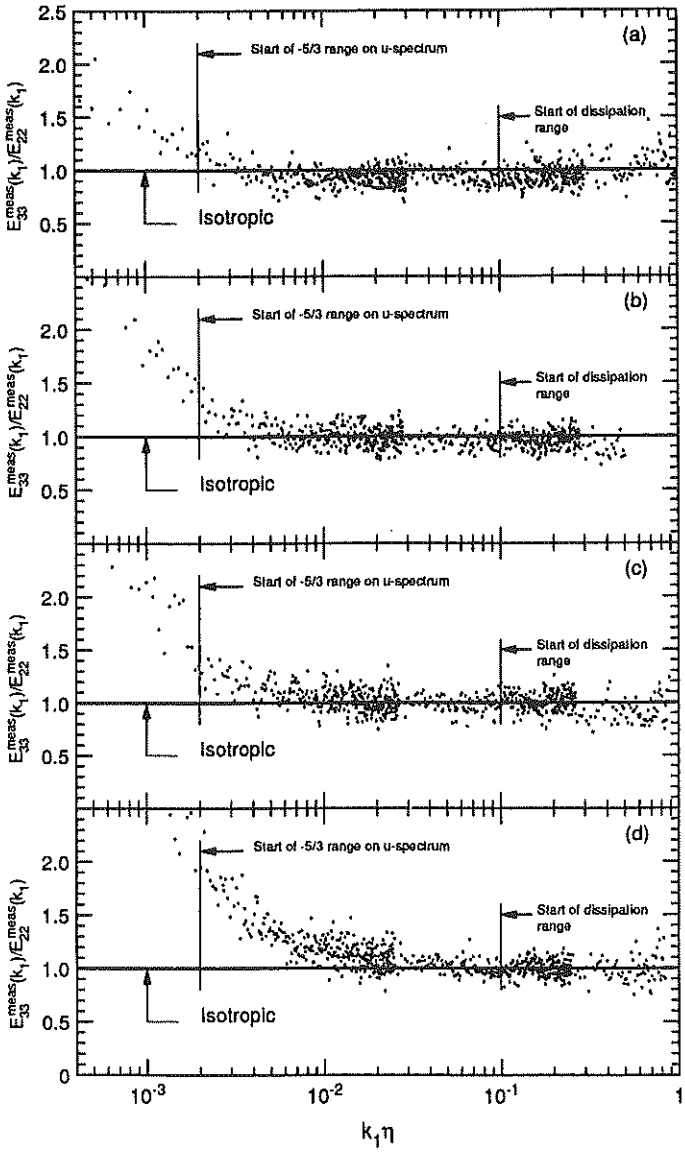

FIGURE 8. Ratios of the measured u_3-spectra to u_2-spectra at different locations in the large extra-strain-rate boundary layer at low Reynolds number. For key to captions for (a)-(d) see Fig. 5.

compared well with the spectra measured by single wires (shown in Fig. 5).

If the motion is isotropic, the transverse spectra $E_{22}(k_1)$ and $E_{33}(k_1)$ are uniquely determined by the longitudinal spectrum $E_{11}(k_1)$ (e.g. Batchelor 1953): $E_{22}(k_1) = E_{33}(k_1) = \frac{1}{2}(1 - k_1\frac{\partial}{\partial k_1})E_{11}(k_1)$. The transverse spectra, $E_{22}^{calc}(k_1)$ and $E_{33}^{calc}(k_1)$, can be calculated from the measured longitudinal spectrum, $E_{11}^{meas}(k_1)$, using the above equation. An anisotropy measure may be defined as $E_{\alpha\alpha}^{calc}(k_1)/E_{\alpha\alpha}^{meas}(k_1)$, where $\alpha = 2$ or 3 corresponds to u_2 or u_3 respectively. These anisotropy measures

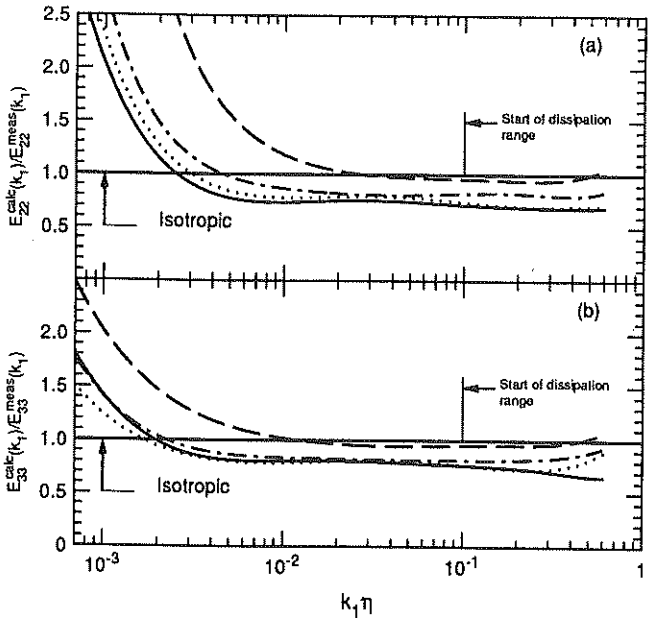

FIGURE 9. Ratios of the calculated to measured transverse spectra at different locations in the large extra-strain-rate boundary layer at low Reynolds number. (a) u_2-ratio; (b) u_3-ratio. ——— , $y = 700$ mm (outer-layer), $R_\lambda \approx 650$; ····· , $y = 500$ mm (around mid-layer), $R_\lambda \approx 820$; —·— , $y = 300$ mm (maximum shear stress), $R_\lambda \approx 800$; ---- , $y = 100$ mm (inner-layer), $R_\lambda \approx 830$.

should be equal to 1.0 in an isotropic flow. We have used the least-squares fit data in Figs. 5, 6, and 7 to calculate these measures, which are plotted against $k_1\eta$ in Fig. 9. These measures clearly show that, as expected from our earlier observations of the compensated spectra, at the inner-layer position, isotropy is satisfied, and when the outer part of the boundary layer is approached, the transverse spectra deviate from the local-isotropy predictions.

We showed (Saddoughi 1993b) that our small-scale measurements in the highly-distorted boundary layer at high Reynolds number followed the local-isotropy predictions. For the same flow at low Reynolds number, isotropy is satisfied in the inner-layer position; however, it appears that in the outer parts of the boundary layer, the small-scale behavior is better described by local-axisymmetry assumption about the streamwise direction (Batchelor 1946) since the measured transverse spectra are equal to each other and they deviate from the isotropy predictions.

The correlation-coefficient spectra, $R_{12}(k_1) \equiv -E_{12}(k_1)/\sqrt{E_{11}(k_1)E_{22}(k_1)}$, are plotted in Fig. 10. In isotropic flow the shear-stress cospectrum, $E_{12}(k_1)$, which satisfies $\int_0^\infty E_{12}(k_1)\,dk_1 = -\overline{u_1u_2}$, is equal to zero. This indicates that the correlation coefficient spectrum should fall to zero at high wavenumbers. This condition should also be satisfied for a locally-axisymmetric flow. As can be seen in Fig. 10, for all the measurement positions in this boundary layer the $R_{12}(k_1)$ spectra drop to zero at high wavenumbers, but as noted before (Saddoughi & Veeravalli 1994),

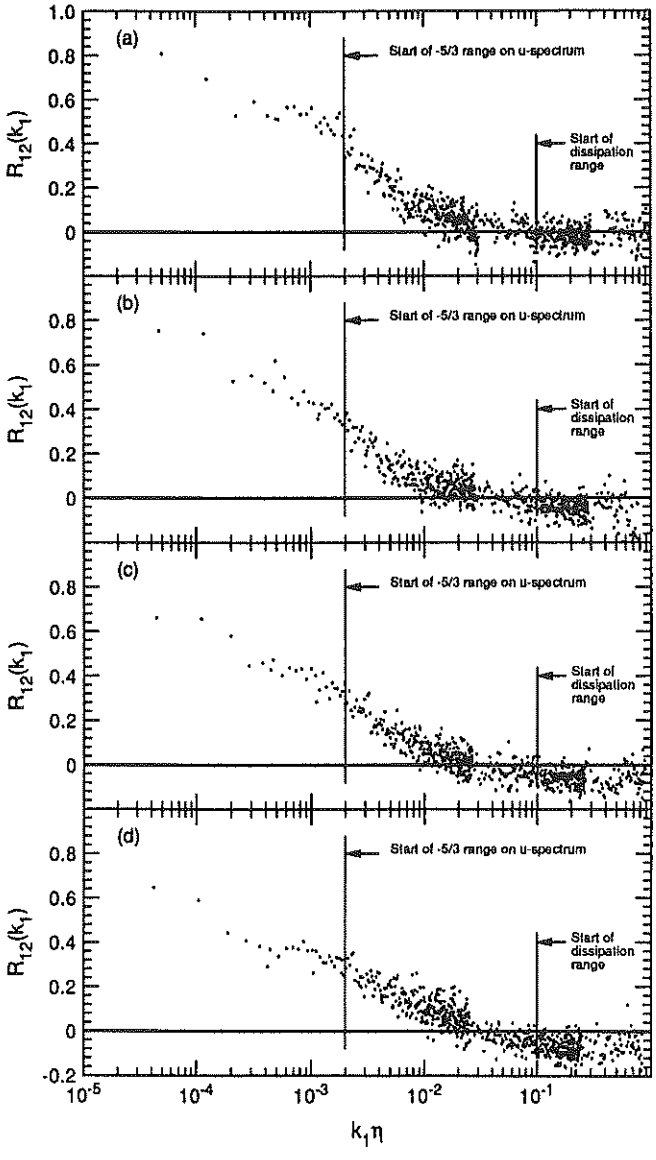

FIGURE 10. Correlation-coefficient spectra obtained at different locations in the large extra-strain-rate boundary layer at low Reynolds number. For key to captions for (a)-(d) see Fig. 5.

both positive and negative values are inferred from the measurements in the high-wavenumber ranges for all the measurement stations. However, in the dissipation ranges of the present case at the measurement locations close to the wall, average values of $R_{12}(k_1)$ appear to be slightly negative. Based on their model for Taylor-hypothesis correction, Wyngaard & Clifford (1977) suggested that the convection velocity fluctuations could alias enough spectral content into the measured cospectrum to make it appear to change sign at large k_1. At the inner-layer station where

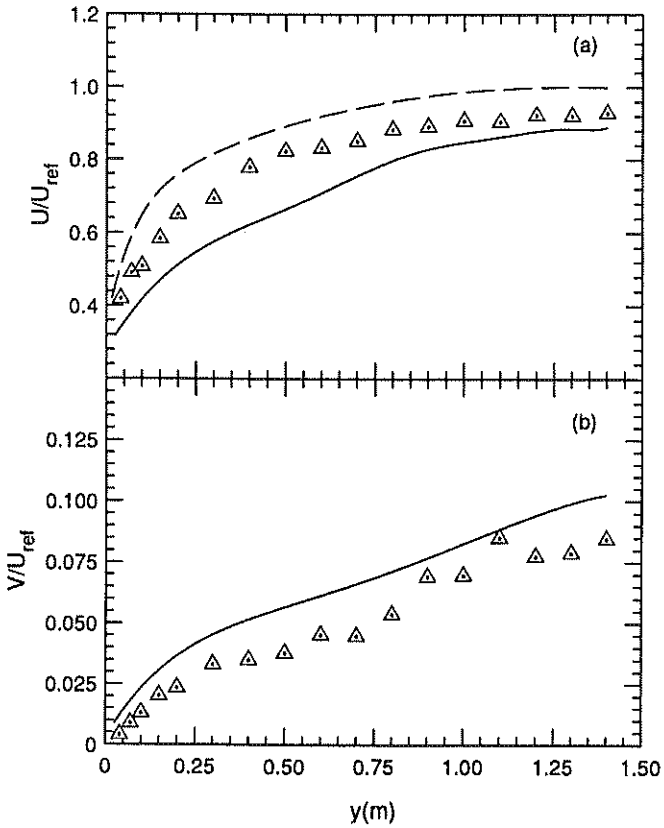

FIGURE 11. Normalized mean-velocity profiles for different boundary layers. (a) U/U_{ref}; (b) V/U_{ref}. ---- , plane boundary layer at low and high Reynolds numbers; ——— , large extra-strain-rate (with F-18) boundary layer at low and high Reynolds numbers; △, small extra-strain-rate (without F-18) boundary layer at low Reynolds number.

the local turbulence intensity for the current experiment is approximately 0.2, the errors arising from the use of Taylor's hypothesis can be large in the dissipation range, and the present data appear to follow the trend suggested by Wyngaard & Clifford (1977).

2.3 Distorted boundary layers: Small extra-strain-rate experiments

In order to isolate the reasons for the deviations of the transverse spectra from the local-isotropy predictions in the outer parts of the distorted boundary layer at low Reynolds number, we repeated our measurements in front of the cylinder after the F-18 aircraft was removed from the 80′ × 120′ wind tunnel.

The normalized profiles of the longitudinal mean velocity, U/U_{ref}, and the vertical velocity component, V/U_{ref}, for this case measured at low Reynolds number, are compared with the profiles obtained for the plane boundary layer and the large extra-strain-rate case (with F-18) in Fig. 11. It is clear that the removal of the F-18 from the wind tunnel reduces the magnitudes of the extra mean strain rates in

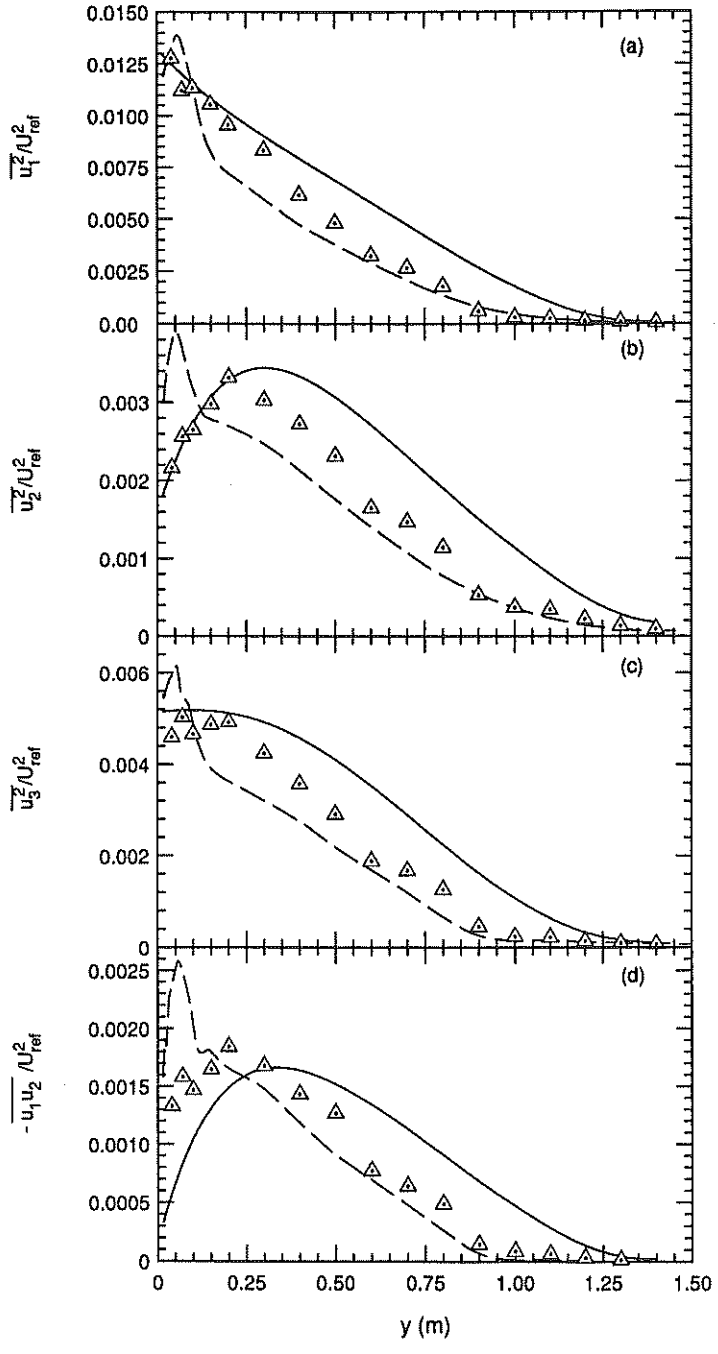

FIGURE 12. Normalized profiles of Reynolds stresses for different boundary layers. (a) $\overline{u_1^2}/U_{ref}^2$, (b) $\overline{u_2^2}/U_{ref}^2$, (c) $\overline{u_3^2}/U_{ref}^2$, (d) $-\overline{u_1u_2}/U_{ref}^2$. For key to symbols see Fig. 11.

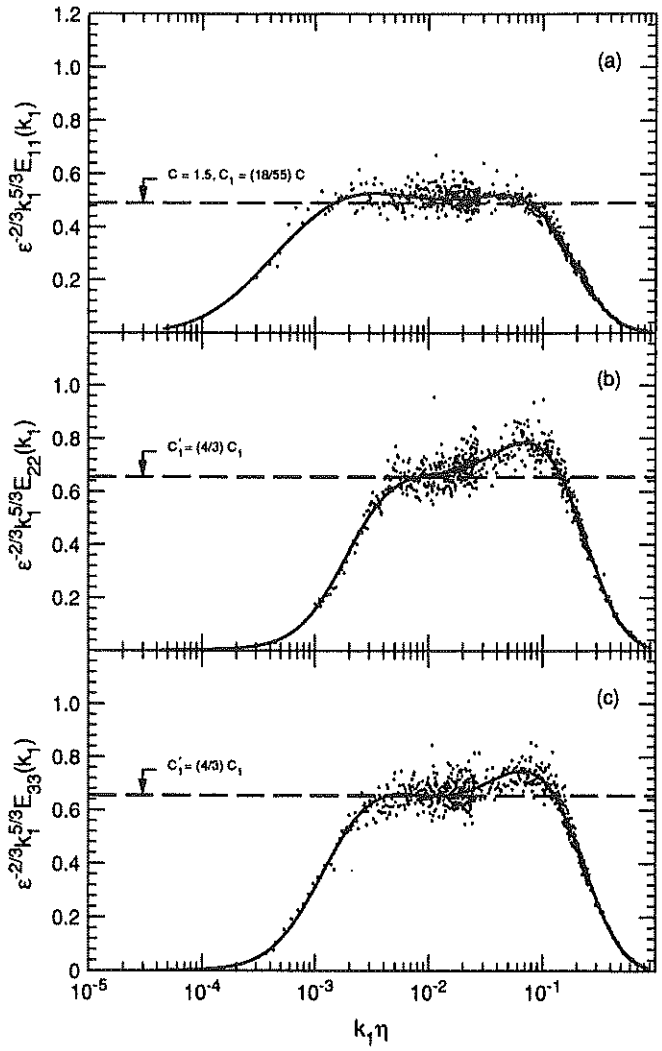

FIGURE 13. Compensated longitudinal and transverse spectra measured at $y = 300$ mm in the small extra-strain-rate boundary layer at low Reynolds number ($R_\lambda \approx 790$). Solid lines are the ninth-order, least-square, log-log polynomial fits to the spectral data. (a) u_1-spectrum; (b) u_2-spectrum; (c) u_3-spectrum.

front of the cylinder. This reduction can be seen also on the profiles of the Reynolds stresses, shown in Fig. 12.

2.3.2 Analysis of small-scale data: low-Reynolds-number case

The compensated spectra of the three components of the velocity taken at $y = 300$ mm, 500 mm, and 700 mm for the low-Reynolds-number case are shown in Figs. 13, 14, and 15 respectively. Recall from Figs. 6 and 7 that the deviations from the

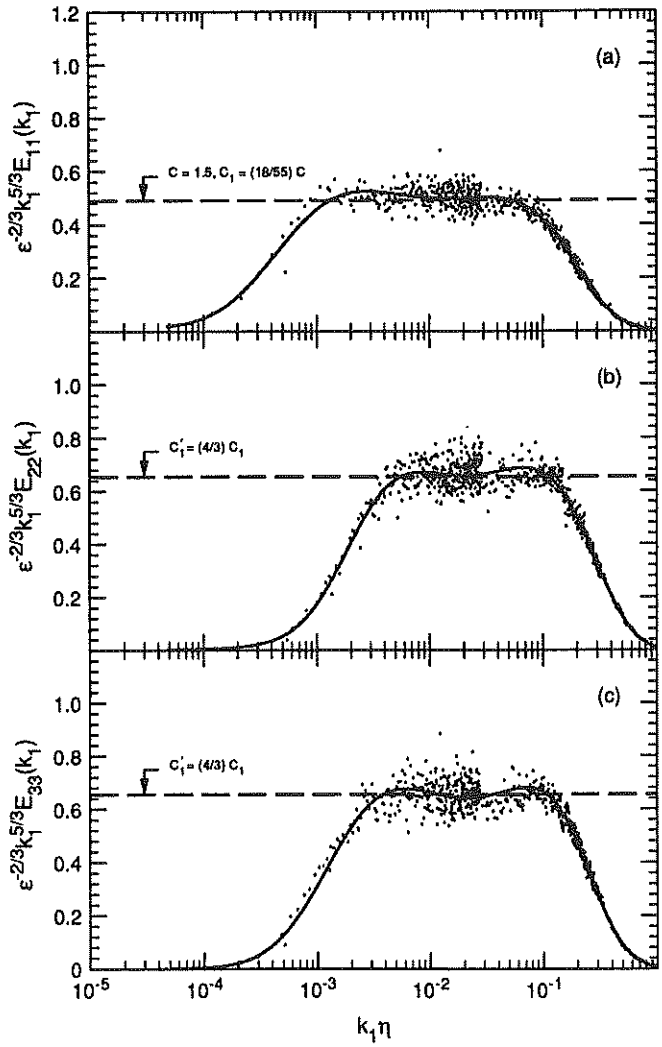

FIGURE 14. Compensated longitudinal and transverse spectra measured at $y =$ 500 mm in the small extra-strain-rate boundary layer at low Reynolds number ($R_\lambda \approx 760$). Solid lines are the ninth-order, least-square, log-log polynomial fits to the spectral data. (a) u_1-spectrum; (b) u_2-spectrum; (c) u_3-spectrum.

small-scale isotropy took place only at these three y locations. However, for the present case, without the presence of the F-18, the transverse spectra at all the measurement stations follow the local-isotropy predictions: i.e. at each station the transverse spectra are equal to each other and are larger than the u_1-spectrum by the 4/3 factor.

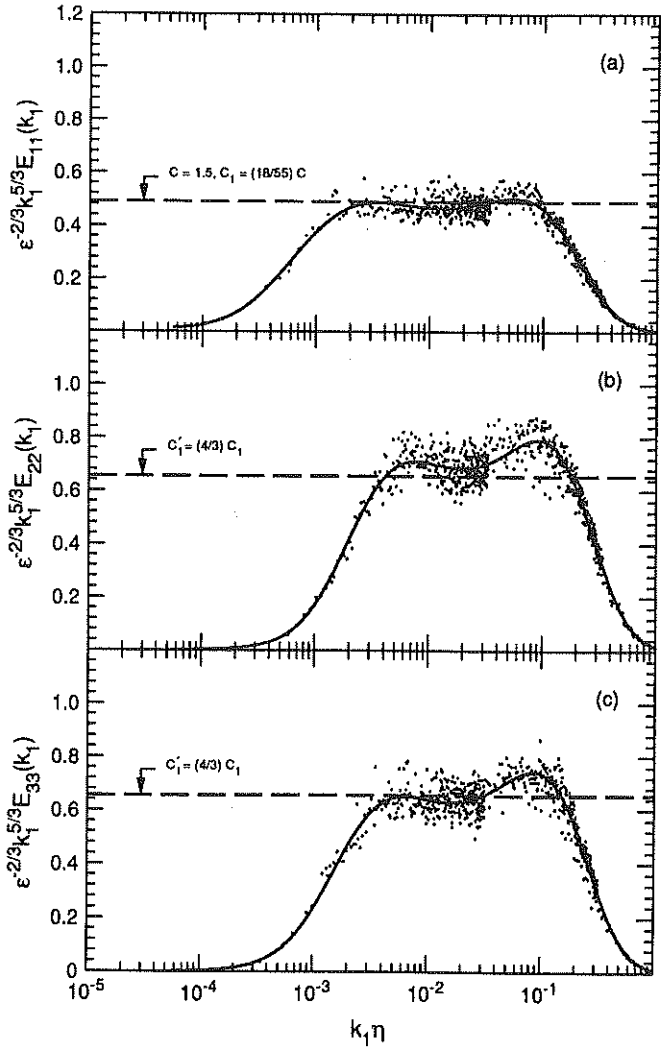

FIGURE 15. Compensated longitudinal and transverse spectra measured at $y = 700$ mm in the small extra-strain-rate boundary layer at low Reynolds number ($R_\lambda \approx 560$). Solid lines are the ninth-order, least-square, log-log polynomial fits to the spectral data. (a) u_1-spectrum; (b) u_2-spectrum; (c) u_3-spectrum.

3. Closure

Further analysis of all the data taken in distorted boundary layers at high and low Reynolds numbers is in progress. However, our complex-flow experiments (see also Saddoughi 1993b) have again highlighted an important fact: as long as the high-Reynolds-number requirement – which is an intrinsic part of the local-isotropy hypothesis – is satisfied, the small-scale structures of turbulent motions become independent of large-scale structures and the mean deformation rate (Kolmogorov 1941).

Acknowledgments

We wish to thank Drs. Fredric Schmitz, James Ross, Wendy Lanser, Gavin Botha, Paul Askins, and Pet Zell of the Full-Scale Aerodynamics Research Division at NASA Ames for their kind cooperation during the experiments.

We wish to thank Professors Bill Reynolds, Parviz Moin, Peter Bradshaw, Bob Rogallo, Javier Jimenez, and Bill George for many valuable discussions of our results.

I am grateful to my wife, Elizabeth, who helped me with the measurements.

REFERENCES

BATCHELOR, G. K. 1946 The theory of axisymmetric turbulence. *Proc R. Soc. Lond.* **A186,** 480-502.

BATCHELOR, G. K. 1953 *The Theory of Homogeneous Turbulence.* Cambridge University Press.

BRADSHAW, P. 1967 The turbulence structure of equilibrium boundary layers. *J. Fluid Mech.* **29,** 625-645.

BRADSHAW, P. 1973 Effects of streamline curvature on turbulent flow. *AGARDograph* **169.**

CORRSIN, S. 1958 On local isotropy in turbulent shear flow. *Report NACA R & M 58B11.*

KOLMOGOROV, A. N. 1941 The local structure of turbulence in incompressible viscous fluid for very large Reynolds numbers. *C. R. Acad. Sci. U.R.S.S.* **30,** 301.

LUMLEY, J. L. 1967 Similarity and the turbulent energy spectrum. *Phys. Fluids.* **10,** 855-858.

MONIN, A. S. & YAGLOM, A. M. 1975 *Statistical Fluid Mechanics, vol. 2. M.I.T. Press.*

SADDOUGHI, S. G. 1993a Local isotropy in high Reynolds number turbulent shear flows. *Annual Research Briefs-1992*, Center for Turbulence Research, Stanford University/NASA Ames. 237-262.

SADDOUGHI, S. G. 1993b Local isotropy in distorted turbulent boundary layers at high Reynolds number. *Annual Research Briefs-1993*, Center for Turbulence Research, Stanford University/NASA Ames. 347-363.

SADDOUGHI, S. G. & JOUBERT, P. N. 1991 Lateral straining of turbulent boundary layers. Part 1. Streamline divergence. *J. Fluid Mech.* **229,** 173-204.

SADDOUGHI, S. G. & VEERAVALLI, S. V. 1994 Local isotropy in turbulent boundary layers at high Reynolds number. *J. Fluid Mech.* **268,** 333-372.

UBEROI, M. S. 1957 Equipartition of energy and local isotropy in turbulent flows. *J. Appl. Phys.* **28,** 1165-1170.

WYNGAARD, J. C. & CLIFFORD, S. F. 1977 Taylor's hypothesis and high-frequency turbulence spectra. *J. Atmos. Sci.* **34,** 922-929.